Retraction Notice

The Editor-in-Chief and the publisher have retracted this article, which was submitted as part of a guest-edited special section. An investigation uncovered evidence of systematic manipulation of the publication process, including compromised peer review. The Editor and publisher no longer have confidence in the results and conclusions of the article.

KF, WS, JK, and KG either did not respond directly or could not be reached.

Image restoration and quantitative metallographic tissue based on machine vision

Keya Fu,[a] Weibo Shi,[b] Jiang Ke,[b] and Kai Guo[c,d,*]

[a]Beihang University, School of Electrical and Information Engineering, Beijing, China
[b]Luoyang Ship Material Research Institute, Luoyang, China
[c]Henan University of Science & Technology, School of Management, Luoyang, China
[d]Collaborative Innovation Center of Nonferrous Metals, Luoyang, China

Abstract. In recent years, with the development of computer image processing technology and quantitative metallography, quantitative metallographic analysis and image restoration based on machine vision image processing have attracted extensive attention. To deeply study the special ability of machine vision technology in metallographic image restoration and quantitative analysis, we adopt a model construction method, parameter design method and comparative analysis method to collect samples and analyze the machine vision system. Through quantitative metallographic organization, based on the progress in artificial neural networks and classification algorithms, a set of analysis system equipment and image restoration algorithm was finally established. The experimental results show that the recognition rate of this method is 5.69% higher than that of method 3, and the overall recognition rate is 5.1% higher than that of method 3, reaching 98.65%. It basically proves the superiority of the image classification algorithm in this paper and also indirectly proves that the system can play a role in the restoration and quantitative analysis of metallographic tissue images. © 2022 SPIE and IS&T [DOI: 10.1117/1.JEI.31.5 .051412]

1 Introduction

From the perspective of materials science, analyzing the relationship between metal structure and properties can effectively predict material properties. Metallographic analysis is an important method for metal research and performance testing. However, the metallographic structure is generally nonuniform on the microscopic level, and multiple measurements in a sufficient field of view are required to ensure the reliability of the data. Machine vision mainly uses computers to simulate human visual functions, extract information from images of objective things, process and understand them, and finally use them for actual detection, measurement, and control.

At present, metallographic analysis mainly relies on professional inspectors with a material science foundation. They observe the metallographic image under the microscope, record its parameters such as structure and grain size, and compare it with a standard metallographic image. It is necessary to combine with computer vision technology, use the efficiency and accuracy of computer vision to process metallographic images, and realize the automation of quantitative metallographic analysis, which has great practical significance and economic value. In the research, a variety of operators are used to process images, and these operators also belong to the category of machine vision.

In fact, it is not uncommon to use machine vision techniques to analyze and process metallographic images. Anisovich and Rumyantseva[1] considered the possibility of applying high-energy effects to metallographic etching. However, the research process has not been made public. Miyazaki et al.[2] undertook various preheating and machining processes on Ti substrates,

---

followed by NaOH and heat treatment. However, this study is largely impractical. Adam et al.[3] discussed the impact of explosive forming projectiles on the armor-piercing process. Unfortunately, there is no conclusive data to support. Wołczyński et al.[4] conducted some metallographic studies on the basis of large forged steel static ingots, but the research content was inconsistent with the final conclusion. Konieczny et al.[5] presented the effect of casting method and anodization parameters on the thickness and structure of the anode layer formed on aluminum alloys. However, there are errors in the study. Uzan et al.[6] aimed to characterize the macro- and microstructure of AlSi10Mg cup-shaped parts produced by additive manufacturing selective laser melting. Unfortunately, the research direction is wrong. Camicia and Timelli reported the effect of grain refinement and cooling rate on the microstructure and mechanical properties of secondary alloys. The results show that the addition of grains produces a fine and uniform grain structure throughout the casting, and this effect is more pronounced in the slow solidification zone. Unfortunately, the research depth is not enough.[7] The data of these studies are not comprehensive, and the results of the studies are still open to question, so they cannot be recognized by the public and thus cannot be popularized and applied.

The innovations of this article are: (1) the improved Mahalanobis distance is used instead of Euclidean distance as the measurement method of similar image blocks. The improved Mahalanobis distance can eliminate the influence of noise to a certain extent, making the clustering results of noisy image blocks more accurate. (2) The calculation method of gray entropy further considers the gray uniformity in the target and background area of the metallographic image. (3) It avoids the binarization of the metallographic image caused by a single algorithm due to different image gray levels. Distortion can deal with metallographic images more effectively and reasonably. Through the above work, the metallographic image restoration and quantitative analysis are more scientific and reliable. (4) Metallographic image analysis uses a special camera to observe a specific sample, and there are five steps: sampling, mosaic, sample grinding, polishing, and erosion of the sample.

2 Implementation Method Based on Machine Vision-Based Metallographic Image Restoration and Quantitative Analysis

2.1 Machine Vision Technology

Machine vision uses computers to simulate the visual function of the human eye,[8,9] extracts information from images or image sequences, and performs shape and motion recognition on three-dimensional (3D) scenes and objects in the objective world.[10]

A typical industrial machine vision application system includes the object under test, light source, optical system, sensing unit, control unit, and signal processing unit, etc., to complete the measurement, detection, identification, and guidance of the object under test, as shown in Fig. 1.[11,12]

As shown from Fig. 1, the charge coupled device (CCD) camera first converts the target object into an optical image signal and then converts it into a digital signal and sends it to the image processing system. The CCD camera is in the security system, and the image generation is mainly from the CCD camera. It can convert light into electric charge and store and transfer the electric charge. The electric charge is taken out to change the voltage, so it is an ideal CCD camera element. The CCD camera has the characteristics of small size, light weight, not affected by magnetic fields, and has the characteristics of antivibration and impact, and is widely used. According to information such as color, brightness, pixel distribution, etc., the characteristics of the target are extracted through various operations. The preset condition judges the output result.[13]

Binocular recognition technology is based on the principle of human eye recognition. Machine vision imaging is similar to human eye imaging. Binocular recognition technology simulates human vision to recognize and process the content to be recognized, as shown in Fig. 2.

It is shown in Fig. 2 that according to the principles of Euclidean geometry and insinuation geometry, each surface can be connected through a homogeneous equation to establish a mathematical model of the camera and the robot.[14] Projection Theorem, also known as Euclidean's
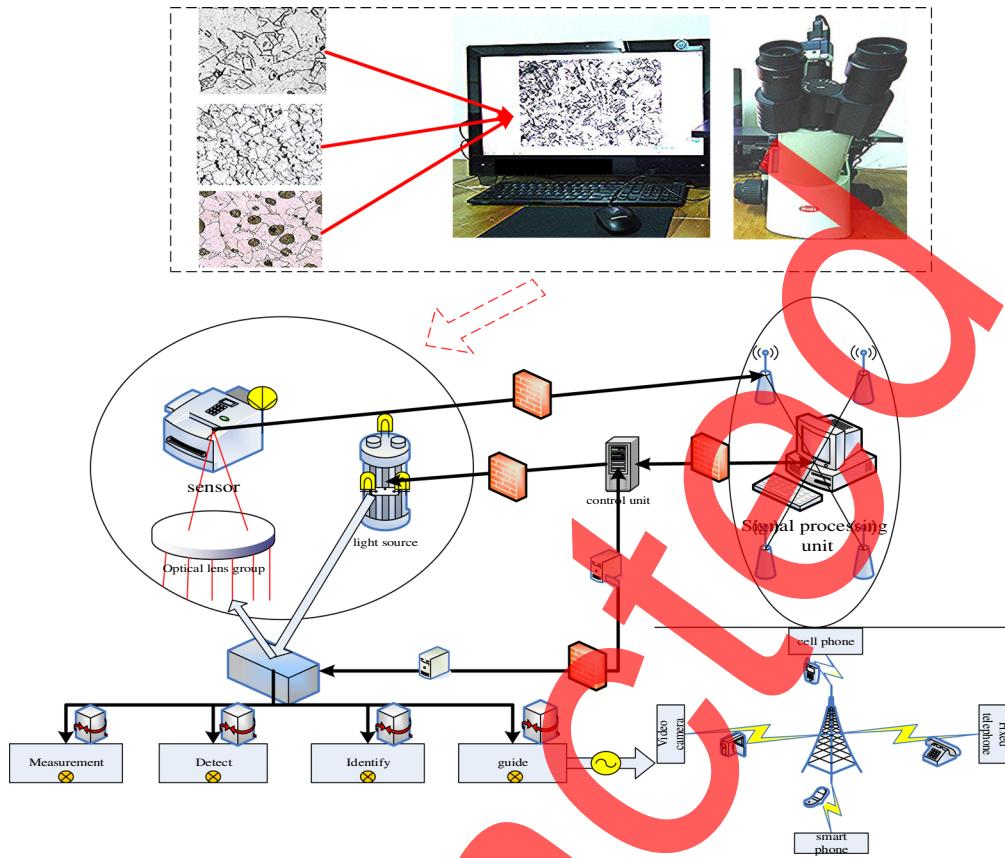
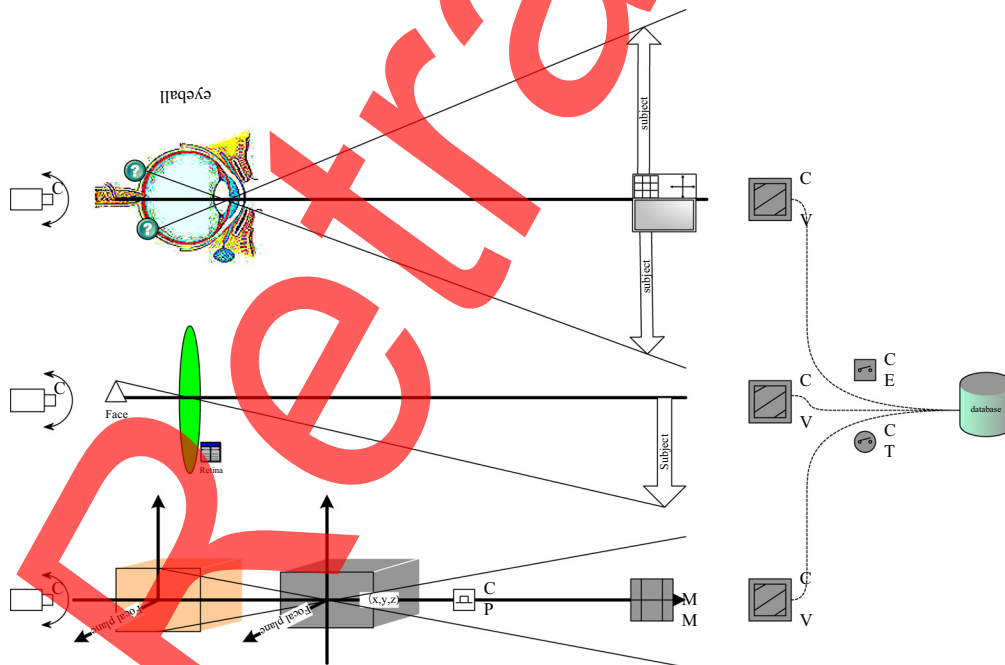**Fig. 1** Typical industrial machine vision system structure.

Fig. 2 Human eye imaging and camera imaging.

Theorem, states: In a right-angled triangle, the height on the hypotenuse is the middle term of the ratio of the projections of the two right-angled sides on the hypotenuse, and each right-angled side is the right-angled side on the hypotenuse. The Projection Theorem is an important theorem in mathematical graph computation:

$$\beta \begin{bmatrix} v \\ m \\ 1 \end{bmatrix} = \begin{bmatrix} (t_a w_a)^{-1} l & 0 & v_0 \\ 0 & w_b^{-1} l & m_0 \\ 0 & 0 & 1 \end{bmatrix} \begin{bmatrix} e_{11} & e_{12} & e_{13} \\ e_{21} & e_{22} & e_{23} \\ e_{31} & e_{32} & e_{33} \end{bmatrix} \begin{bmatrix} a_d \\ b_d \\ c_d \\ 1 \end{bmatrix}, \tag{1}$$

where l is the internal parameter, and e_{11} is the external parameter.[15]

2.2 Metallographic and Metallographic Analysis

The broader content of metallography or metallographic processing is the composition of metals and metalloids and their relationship to many physical properties.[16] Using the principle of quantitative metallography, the 3D spatial morphology of the alloy structure is determined by the measurement and calculation of the metallographic microstructure of the ground surface or thin film of the two-dimensional metallographic sample, thereby establishing the quantitative relationship among the alloy composition, structure, and properties. Although the optical microscope has the advantages of simplicity and convenience, the recognition degree is not high, and it can only observe the micron-level standard fine section of the structure.[17] To obtain a higher recognition rate to observe finer structural components, a new generation of electron microscopes was successfully invented at the beginning of the last century.[18]

Quantitative metallographic calculation mainly includes two steps.[19,20] The first is to measure and calculate the characteristic data of the sample image or the mapped image and then use the formula to evolve the characteristic parameters into the required 3D characteristic parameters, that is, the spatial properties of the reduced alloy structure.[21] At home and abroad, quantitative image analyzer is the most widely used analysis tool. The detailed composition of the tool model is shown in Fig. 3;

As shown in Fig. 3, the acquisition of metallographic images is mainly the process of sample preparation and screenshots. After the polished sample alloy is immersed in the "etching solution," irregular shape differences are formed due to various parameters.[22] Metallographic quantitative analysis tools are suitable for various production enterprises related to metal material products, such as steel production, shipbuilding, automobile manufacturing, aircraft manufacturing, high-pressure vessels, electrical devices, bearings, standard parts, hardware and textile accessories, and instrumentation accessories.

Adjust the position of the light spot and components so the light hits the center of the vertical device entrance so the resulting brightness is uniform. Place the prepared sample evenly on the observer's stage with its plane perpendicular to the microscope light.[23] The wiring diagram of the equipment is shown in Fig. 4.

As shown in Fig. 4, the main hardware devices used are metallographic microscopes and digital cameras. Digital metallographic microscope is a high-tech product developed by perfectly combining optical microscope technology, photoelectric conversion technology, and computer image
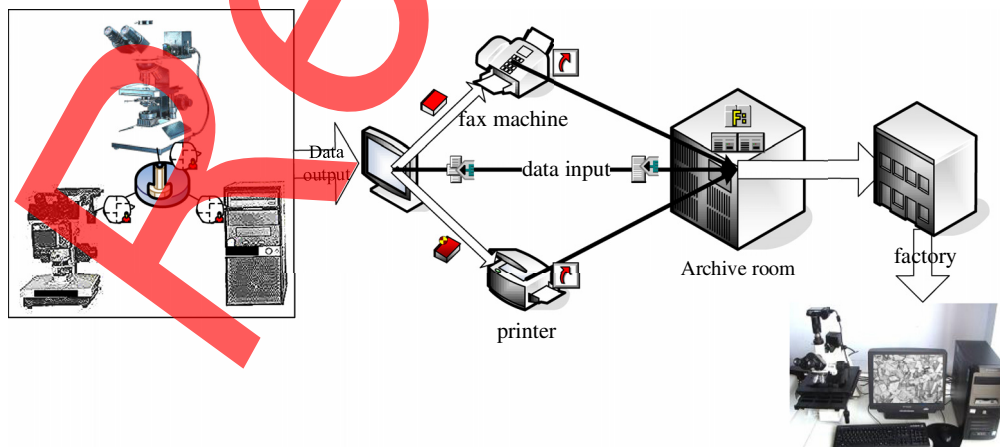

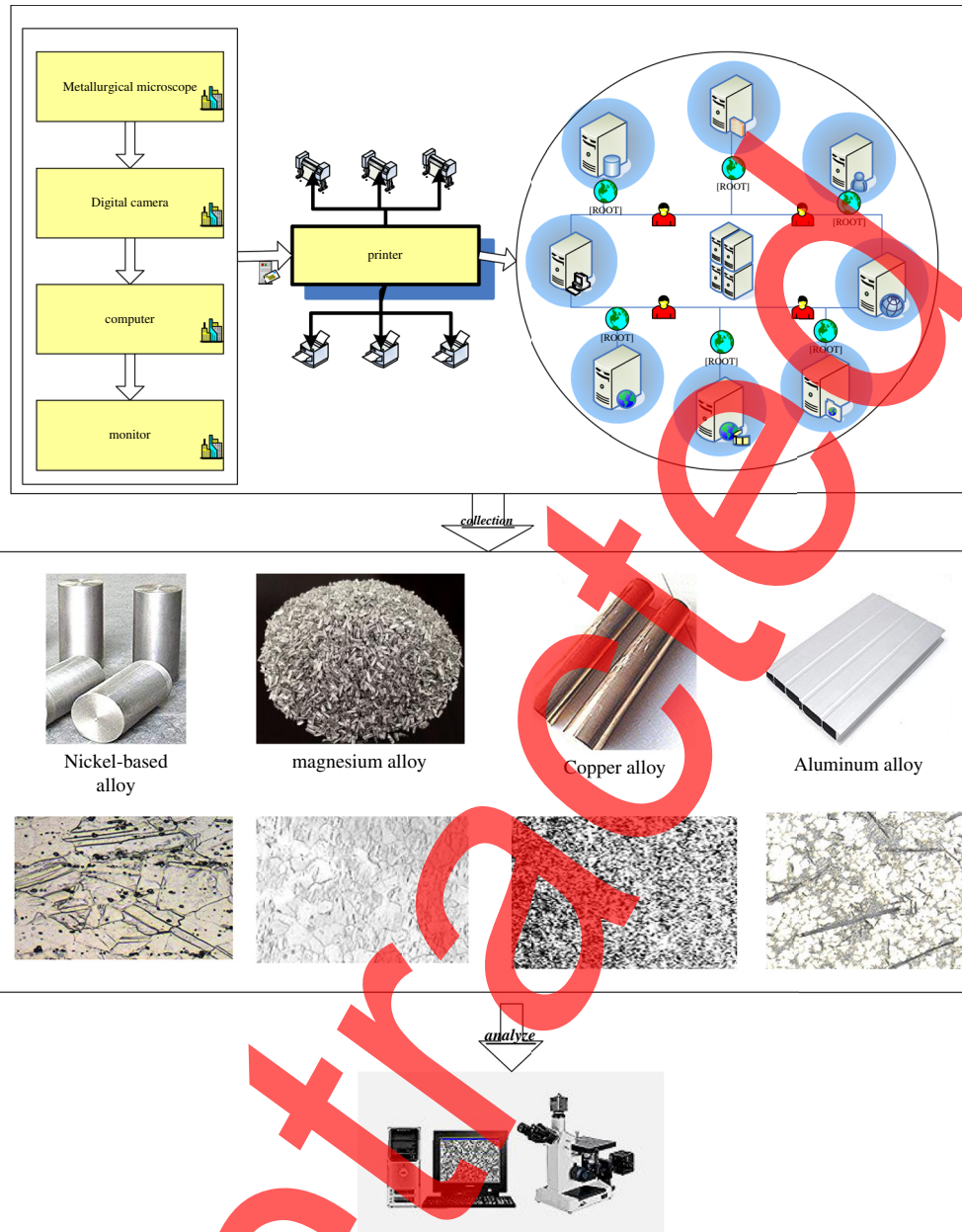**Fig. 3** Metallographic quantitative analysis tool.

Fig. 4 Connection diagram of image acquisition equipment.

processing technology. The internal structure of metallic materials can only be observed under a microscope. After the image is acquired, the image is processed. Generally speaking, image processing technology uses mobile network terminals or other system hardware to perform some algorithmic processing on the electrical signals converted from image information to improve the practical usability of images.[24–26]

Mahalanobis distance is a new method proposed by Indian scholars to measure the correlation of samples. The Mahalanobis distance makes up for the defect that the traditional Euclidean distance ignores the correlation between samples, and the Mahalanobis distance is better than the Euclidean distance in the image patch matching of edge and texture regions. In this paper, using Mahalanobis distance instead of Euclidean distance can better measure the similarity of image patches and optimize the grouping results.

Assuming that two column vectors are expressed as a_u and a_k, their Mahalanobis distance is expressed as

$$w_{u,k} = \sqrt{(a_u - a_k)^\rho \sum^{-1}(a_u - a_k)}, \tag{2}$$

$$\sum = (a_{u,k} - a_n)(a_{u,k} - a_n)^s + (b_u - b_k)\sum_{u=1}(x_a + x_b), \tag{3}$$

where $\sum a$ is the covariance matrix of a_u and a_k.

Since the traditional Mahalanobis distance needs to solve the inverse of the covariance matrix of the sample, when the inverse of the covariance matrix does not exist, the Mahalanobis distance is unstable. To solve this problem, this paper uses the M-P generalized inverse to replace the inverse of the covariance matrix:

$$\sum^{+} = m\begin{pmatrix} t^{-1} & 0 \\ 0 & 0 \end{pmatrix}v^g + v\begin{pmatrix} t & 0 \\ 0 & 1 \end{pmatrix}m^g, \tag{4}$$

where v and m are the unitary matrices.

In practice, β_1 is much larger than $\beta_1(u = 2, \cdots e)$, and the singular value can be approximately expressed as

$$\sum^{+} = \frac{1}{\beta_1}m\begin{pmatrix} 0.1 & \cdots & 0.1 \\ \vdots & \ddots & \vdots \\ 0.1 & \cdots & 0.1 \end{pmatrix}v^g = \frac{1}{\beta_1^2}\sum^g = \frac{1}{\beta_1^2}\sum a. \tag{5}$$

Combining Eq. (5) with Eq. (2), the improved calculation equation is

$$w_{u,k} = \frac{1}{\beta_1}\sqrt{(a_u - a_k)^s \sum(a_u - a_k)}. \tag{6}$$

In the equation, $w_{u,k}$ is the optimized algorithm equation. Approximate calculation of the singular value of the covariance matrix not only reduces the amount of calculation but also eliminates some noise interference. Using Mahalanobis distance instead of Euclidean distance can be more accurate to measure the similarity between samples, the grouping results are more accurate.[27]

In the PCA domain, the energy of the noise signal is evenly distributed in the entire data set, while the energy of the clean image is mainly distributed in a small part of the data set. By mapping the image block samples to the PCA domain, the noise and the clean image can be effectively distinguished.

Cluster the Gaussian mixture model to obtain a sample matrix of similar blocks:

$$b = [b_1^s, b_2^s, \cdots, b_n^s]^s + \overline{b_u}b_u - \eta_u. \tag{7}$$

First, uniform processing is performed on each unit of the sample queue b; the processed image model can still be expressed in the form of $\overline{b} = \overline{a} + m$:

$$\eta_u = \frac{1}{o}\sum_{u=1}^{o} b_u^k, \quad u = 1,2,3,\cdots,n, \tag{8}$$

$$\alpha^s \sum_{\overline{a}} \alpha = \begin{pmatrix} \beta_1 - \vartheta^2 & 0.1 & 0.1 \\ \cdots & 0.1 & \ldots \\ 0.1 & 0.1 & \beta_n - \vartheta^2 \end{pmatrix}. \tag{9}$$

Map the sample to the PCA domain, which is $\overline{\overline{b}} = \alpha^s\overline{b}, \overline{\overline{a}} = \alpha^s\overline{a}, \overline{\overline{m}} = \alpha^s\overline{m}$. Use the following equation to linearly transform each row of $\overline{\overline{b}}$:

$$\overline{\overline{b_g}} = \frac{\beta_g - \vartheta^2}{\beta_g}\overline{\overline{b}}_g, \quad g = 1,2,\cdots,n, \tag{10}$$

$$\overline{\overline{b^=}} = [\overline{\overline{b_1^-}}^s, \overline{\overline{b_2^-}}^s, \cdots, \overline{\overline{b_n^-}}]^s + \left[\sum_{u=1}^{h_k} a + b\right]. \tag{11}$$

The above method is applied to all samples after GMM clustering, and the denoised image can be obtained. This article will use two stages to remove noise. After the first stage of denoising, the image $\overline{u}$ is obtained, and the noise standard deviation is updated by Eq. (11):

$$\vartheta_2 = z_m \sqrt{\vartheta^2 - \frac{1}{n * o} \|u_m - \overline{u}\|_2^2}. \tag{12}$$

In the equation, z_m is a normal number less than 0.5, ϑ is the noise standard deviation of the noisy image u_b, and the size of u_m is $n * o$.; Fig. 5 zooms in on a spheroidal graphite area in the metallographic image of cast iron.

As shown in Fig. 5, most denoising algorithms search for similar image patches within the neighborhood. In this paper, the Gaussian mixture model is used to cluster the global image patches, the improved Mahalanobis distance is used to measure the similarity of different image patches to better measure the similarity of image patches, and the structural information of external natural images is used to guide noise images. A mixture model represents the probability distribution of the observed data in the population, which is a mixture of K subdistributions. The clustering of blocks makes PCA denoising based on a more complete orthogonal transform basis.

The exponential gray scale entropy of the target class z_p is

$$g_p(s, t) = [g_{pu}(s, t), g_{pk}(s, t)]^s + \sum_{u=0}^{s} \sum_{k=0}^{t} g(u, k). \tag{13}$$

To make the expression easy to understand, simplify the intermediate variables in the above equation, let,

$$\begin{cases} v_{pu}(s, t) = \sum_{u=0}^{s} \sum_{k=0}^{t} g(u, k) * u \\ v_{pk}(s, t) = \sum_{u=0}^{s} \sum_{k=0}^{t} g(u, k) * k \end{cases}. \tag{14}$$
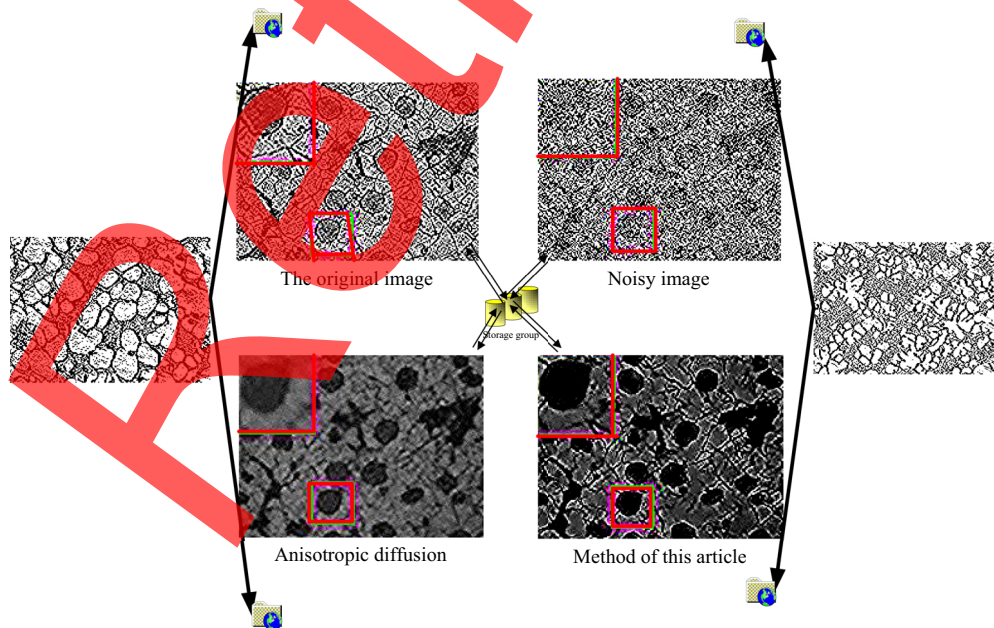

Fig. 5 Comparison of denoising results of nodular cast iron images.

Then, the sum $g(s, t)$ of the exponential grayscale entropy of the target class and the background class of the image is

$$g(s, t) = \sum_{k=1}^{i=1} \sum_{k=0}^{t} g(u, k) \frac{u}{v_{yu}(s, t)} uzi \left(1 - \frac{u}{v_{yu}(s, t)}\right). \quad (15)$$

When $\gamma(s, t)$ reaches the maximum, that is, the exponential gray scale entropy of the image reaches the maximum, the corresponding (s, t) is the optimal segmentation threshold:

$$(s', t') = xeh \min_{\substack{0 < t < i-1 \\ 0 < t < h-1}} \{\gamma(s, t)\}. \quad (16)$$

In the equation, γ is the average entropy value.

In the image classification task, the network assigns a label (or category) to each input image. In this case, you will want to assign a category to each pixel of the image. This task is called segmentation. A segmentation model will return more detailed information about the image. What we use here is an improved U-Net network model. A U-Net consists of an encoder (down sampler) and decoder (up sampler). This paper proposes the recurrent U-Net model and the recurrent residual U-Net model on the basis of U-Net, which are called RU-Net and R2U-Net, respectively. They have the following advantages:

First, when training deep architecture, residual units will help.

Second, the cyclic residual convolutional layer is used for feature accumulation to ensure a better feature representation of the segmentation task.

Third, it allows the author to design a better U-Net architecture with the same number of network parameters and better performance for medical image segmentation.

2.3 Image Restoration

Image restoration is a long-term research content in the field of image processing. Early restoration algorithms were mainly based on some basic mathematical theories and methods designed for image restoration algorithms. To improve the adaptability of the algorithm, regularization methods are widely used in the field of image restoration. The image degradation and restoration process are shown in Fig. 6.

It is shown in Fig. 6 that, mathematically, the image degradation process can be expressed as

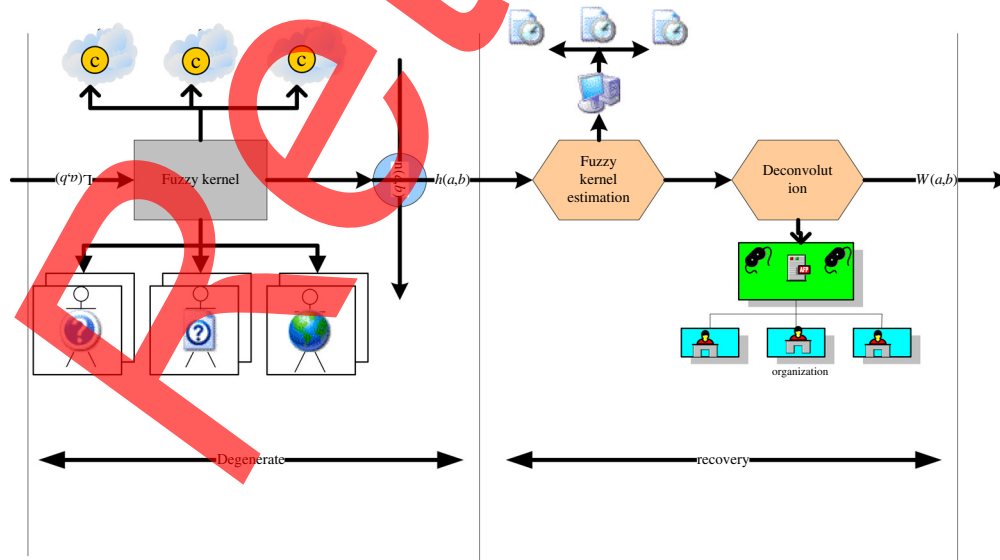$$h(a, b) = l(a, b) * g(a, b) + o(a, b). \quad (17)$$

Fig. 6 Image degradation and recovery process.

In the equation, $h(a, b)$ degenerate image, $l(a, b)$ is the original image, $g(a, b)$ is the blur kernel, that is, the point spread function, and $o(a, b)$ is the additive noise. Image restoration is a process of approximately solving $l(a, b)$ by estimating $g(a, b)$ and $o(a, b)$. Considering the huge amount of computation of spatial deconvolution, it is usually necessary to convert the image signal to the frequency domain using fast Fourier transform to solve Eq. (17). The core problem is to perform inverse filtering in the frequency domain:

$$u(a, b) = l^{-1}\left(\frac{h(v, m)}{\hat{g}(v, m)}\right) + l\left(\frac{h}{g}\right), \tag{18}$$

where $u(a, b)$ is the approximate solution of $l(a, b)$ in the frequency domain, $h(v, m)$ is the frequency domain representation of the degraded image $h(a, b)$, and $\hat{g}(v, m)$ is the estimation of the point spread function value, that is, the frequency domain representation of the estimated fuzzy kernel:

$$\hat{g}(v, m) = g(v, m) + \Delta g(v, m) + \prod_{o_p}^{u=0, i=1} (v, m), \tag{19}$$

where $g(v, m)$ is the point spread function of the actual degradation process, and $\Delta g(v, m)$ is the estimation error of the point spread function. Due to the morbidity of g, even a small disturbance will seriously affect the solution of $u(a, b)$. From Eqs. (18) and (19), it can be seen that the existing disturbances mainly include noise $o(a, b)$ and the estimated error $\Delta g(v, m)$.

In practical applications, there are many types of image restoration algorithms, among which the most widely used is maximum likelihood estimation:

$$k(\hat{h}, \beta) = |f\hat{h}| + \beta ||l - g\hat{h}| - \|o\|^2|, \tag{20}$$

$$\hat{h} = \left(g^s g + \frac{1}{\beta} m^s m\right)^{-1} g^s l - e p q_s^d. \tag{21}$$

In the equation, β is a constant and satisfies the constraints. In practical applications, the Laplace operator is usually selected as m:

$$\hat{h}(v, m) = \left|\frac{1}{g(v, m)} \frac{|g(v, m)|^2}{|g(v, m)|^2 + 1/\beta |m_i(v, m)|^2}\right| h(v, m). \tag{22}$$

In the equation, v and m both take constant values, and Tik is a restoration method based on the smoothness measure. Since the second-order differential is sensitive to the image noise response, it has a good suppression effect on the isolated noise during the restoration process and avoids the point spread function to amplify the noise.

3 Experiments and Conclusions Based on the Design and Implementation Method of Metallographic Tissue Image Restoration and Quantitative Analysis Based on Machine Vision

3.1 Metallographic Sample Preparation

Metallographic image analysis uses a dedicated camera to observe a specific sample and has a total of five steps. From sample extraction to subsequent processing, the final sample should have: representative tissue, no artifacts, real tissue, no wear marks, pockmarks or water marks, etc. The specific steps are shown in Table 1.

After making the samples, we can do the next step of research.

Table 1 Preparation steps of metallographic samples.

Step	Step description	Preparation accuracy (%)	Error requirement
Sampling	Cut out	99.6	<0.1
Mosaic	Bakelite inlay	99.5	<0.05
Grinding of samples	Pregrinding machine for fine grinding	99.1	<0.01
Polishing	Remove wear marks	99	<0.025
Erosion of the specimen	4% nitric acid alcohol solution	99.8	<0.5

3.2 *System Software Platform Selection*

The software system functions include drivers for cameras and image capture cards, as well as a human–computer interaction interface for the user's convenience. Due to the large amount of image data, the system structure and image processing modules must be reasonably arranged. Divide. The detailed software parameter diagram is shown in Table 2.

The operators mainly included in the edge detection module are introduced as shown in Table 3.

3.3 *Project Realization Parameter Requirements*

In this project, the t1 processing board is used as the image processing module, and 1.2 million gate-level FPs are added to implement simple image processing algorithms on the basis of it, and an image acquisition circuit is provided. The appearance adopts PCI bus full-length card, which is connected with the chip through the bus to realize the image transmission and display function. The specific content is shown in Table 4.

The detailed parameter introduction of the circuit used in the system is shown in Table 5.

Table 2 System development software.

Develop software	Production company	Development tools	Task	Data pseudoaccuracy	Reliability
Visual	Pt G	Bumblebee2	Image acquisition	$P > 0.05$	90.9%
C++	Xe P	Parallel binocular	Camera calibration	$P > 0.05$	92.5%
XP6.0	Us E	Camera	Image processing	$P > 0.025$	93.6%

Table 3 Introduction to the operators mainly included in the edge detection module.

Operator introduction	Operator requirements	Detection target	Alloy size (cm)
Rob	6.63 per/s	Copper alloy	601×14
Sob	5.52 per/s	Aluminum alloy	558×10
Pwt	6.32 per/s	Ferroalloy	524×11
Kir	2.52 per/s	Magnesium alloy	513×32
G-L	4.49 per/s	Tungsten alloy	487×22

Table 4 Module content.

Classification	Require	Unit	Parameter source
Processor	T1	TMS300	EAA 100
Internal clock	280 MHz	3.1 ns	ST 305
Calculating speed	2200 MIPS	C6120	UD 280
On-chip RAM	14 KB	L1	XXB 310

Table 5 Circuit introduction.

Circuit parameters	Data	Data accuracy	Actual standard
Operating voltage	3.0 V	93.3%	1.4 V
Guide way	2.2 V	94.5%	1.0 V
External bus	29 MHz	95.4%	20 MHz
EMIF bus	30 bit	93.8%	15 bit

3.4 Image Restoration Results

The net smelting recovery (NSR) value means the value of recoverable metal per unit of ore after deducting smelting and transportation costs. Figure 7 shows the use of Wiener filtering to restore the image and then uses the peak signal-to-noise ratio (PSNR) and structural similarity (SSIM) to evaluate the restored image respectively, where the abscissa is the restoration process using different NSR values as restoration parameters, and the ordinate is the evaluation results of PSNR and SSIM, respectively. The essence of Wiener filtering is to minimize the mean square of the estimation error (defined as the difference between the expected response and the actual output of the filter). The specific evaluation values are shown in the figure.

It is shown in Fig. 7 that with the increase of NSR value, the two evaluation results gradually become flat, PNSR is stable at 17.6, SSIM is stable at 0.405, but it can be seen from the actual situation that the restored image still contains a lot of noise ringing. The effect is more serious with the change of NSR value, but the SSIM evaluation results tend to be flat, which proves that the SSIM algorithm can provide effective evaluation results for the image ringing effect.
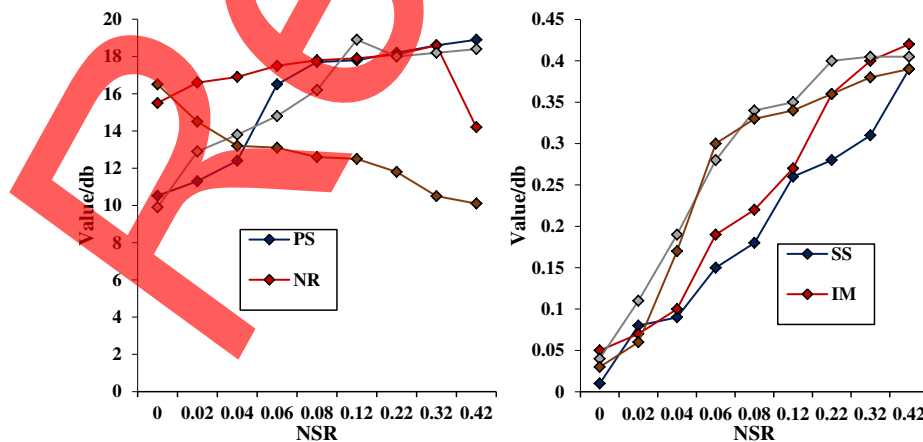

Fig. 7 Image quality evaluation curve after restoration of Wiener filter.
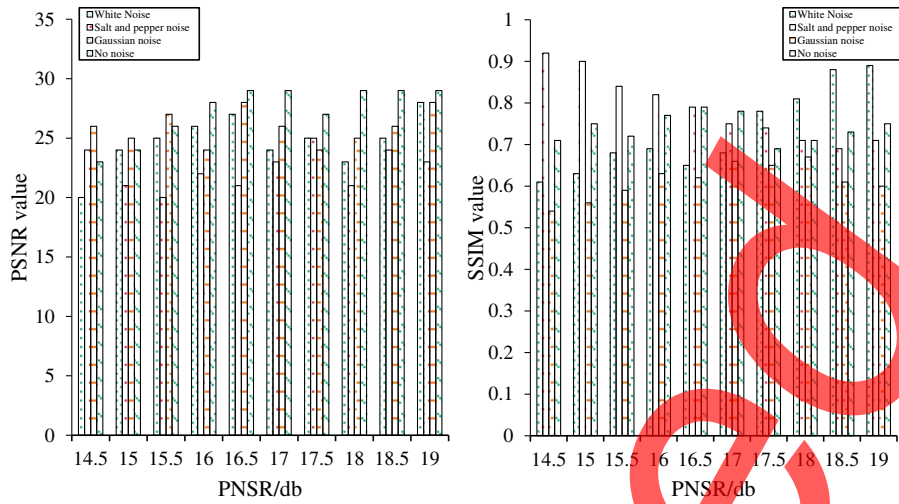
Fig. 8 Baboon quality evaluation curve.

To obtain the restoration effect of various algorithms on different scenes and to verify the sensitivity and applicability of the algorithm to different image contents, 120 test sample images containing rich edge and texture information were selected for the sample content, such as portraits, still lifes, landscapes, and remote sensing. Figure 8(a) shows the evaluation curve obtained after adding different types of noise (white noise, salt and pepper noise, and Gaussian noise) and using the Wiener filter restoration algorithm to restore the image. Figure 8(b) shows the optimized evaluation curve. The coordinate is the evaluation result after adding different types of noise to the standard original image, and the ordinate is the image quality evaluation result curve after the image is restored by different algorithms.

From the evaluation curve in Fig. 8, it can be seen that when the noise is serious, the image blurring changes drastically, and the image restoration effect drops sharply, especially when the PSNR value of the added noise is lower than 15, the change is particularly obvious. PSNR is an objective standard for evaluating images. It has limitations and is generally used for an engineering project between the maximum signal and background noise. The experimental data also verify the algorithm in this paper.

3.5 Quantitative Analysis Results

The algorithm proposed in this paper is tested on a large number of images. Figure 9 shows the average time-consuming and corresponding optimal thresholds of the traditional algorithm, the transfer algorithm, and the algorithm in this paper.
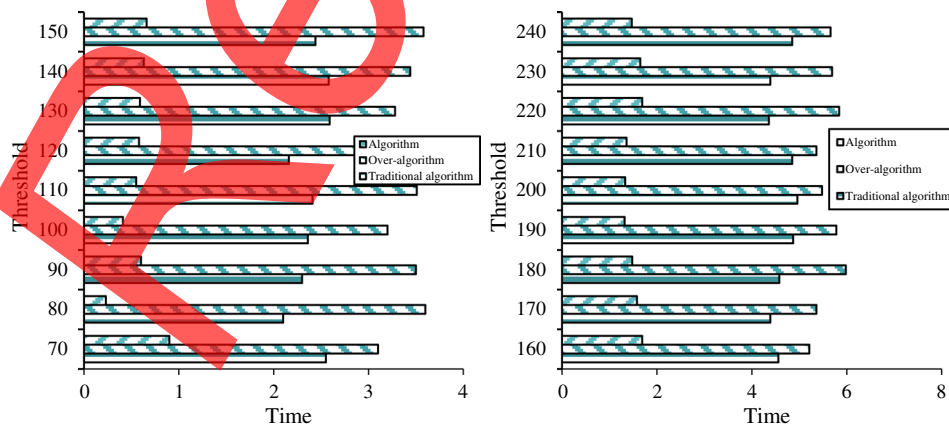

Fig. 9 Comparison of optimal thresholds and time-consuming of different segmentation algorithms.
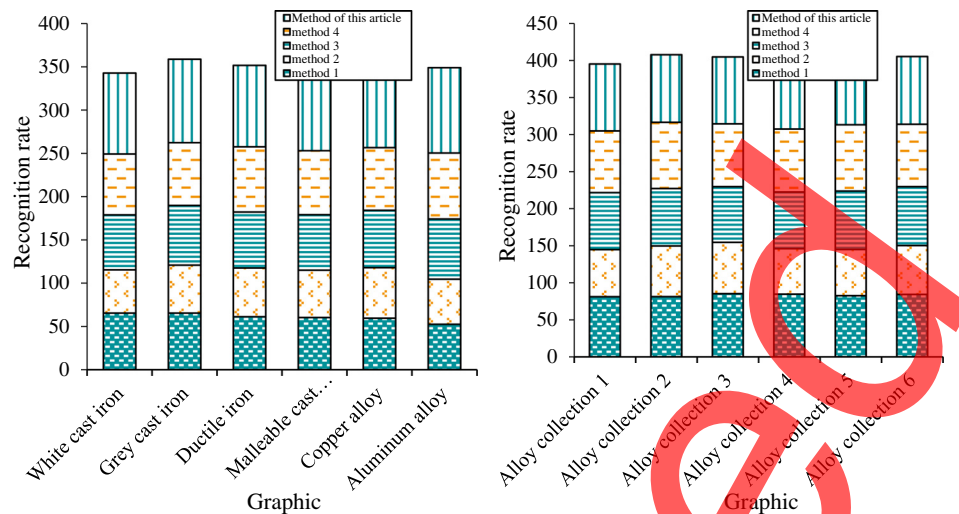
Fig. 10 Classification results of five automatic classification methods.

As shown in Fig. 9, the algorithm in this paper uses the chaotic sequence based on Tent map to improve the local search process, helping the algorithm to get away from the local optimal value and find the global optimal solution faster. A chaotic sequence is an irregular motion that occurs in a deterministic system. Compared with the traditional algorithm and the transfer algorithm, the algorithm in this paper can save 60% to 80% of the time.

The experimental images are from the Do metallographic library, which collects metallographic images of four types of cast iron (white cast iron, gray cast iron, ductile iron, and malleable cast iron). Each type of image consists of three cast iron metallographic images at different scales. The scale includes 100 images of size 80*80, totaling 1200 metallographic images of cast iron. For the convenience of description, the above comparison methods are named as method 1, method 2, method 3, and method 4 in turn. Figure 10 shows the experimental results for the five methods.

It is shown in Fig. 10 that the shape features of cast iron and gray cast iron are more prominent, so the recognition rate is higher in the metallographic images of the four cast irons. Method 3 has the lowest average recognition rate. The recognition rates are only 65.8% and 29.8%, respectively. The recognition rate of this method is 5.69% higher than that of method 3, and the overall recognition rate is 5.1% higher than that of method 3, reaching 98.65%.

4 Discussion

Looking forward to all current related research, scholars worldwide have carried out extensive and in-depth research on metallographic quantitative analysis and image restoration, created numerous metallographic structure analysis systems, and achieved many advances, but there are still shortcomings that need further work. Further research needs are mainly reflected in the following aspects:

(1) Under the current situation of metallographic structure research, it can be seen that there are many types of metallographic analysis instruments, and most of them have their own applicable objects, such as ductile iron grade evaluation, metallographic structure identification, etc. Metallographic analysis systems for alloys are rare. This alloy-centric system was developed from an existing system.

(2) According to the current progress of metallographic analysis, although semisolid metallographic analysis software has been developed, there are still problems such as simple procedures, limited algorithms and methods, and the accuracy and intelligence of quantitative analysis are not very high. The internal structure of the metal structure is intricate, and the image analysis method of the microstructure is still being perfected.

5 Conclusions

In this paper, the digital image restoration part of the machine vision-assisted quantitative metallographic analysis system is deeply studied. On the basis of previous research, a series of improvement methods are proposed for the existing problems. To explore whether machine vision technology can play a role in metallographic image processing, a variety of scientific research methods are used in this paper, such as experimental comparison setting method. In the experiments, we first use Wiener filtering to restore the image and then use PSNR and SSIM, respectively. For the evaluation curve of the restored image, it can be seen that with the increase of the NSR value, the two evaluation results gradually become flat. PNSR is stable at 17.6 and SSIM is stable at 0.405. We found that our algorithm can save 60% to 80% of the time compared to traditional algorithms and transition algorithms.

Acknowledgments

References

1. A. G. Anisovich and I. N. Rumyantseva, "Validity of using high-energy fluxes for the metallographic revelation of the structure," *Surf. Eng. Appl. Electrochem.* **52**(3), 242–249 (2016).
2. T. Miyazaki et al., "Effect of metallographic structure and machining process on the apatite-forming ability of sodium hydroxide- and heat-treated titanium," *Biomed. Mater. Eng.* **29**(1), 109–118 (2018).
3. K. Adam et al., "Metallographic analysis of piercing armor plate by explosively formed projectiles," *Arch. Civil Mech. Eng.* **18**(4), 1686–1697 (2018).
4. W. Wołczyński et al., "Structural zones in large static ingot. forecasts for continuously cast brass ingot," *Arch. Found. Eng.* **16**(3), 141–146 (2016).
5. J. Konieczny et al., "Influence of aluminium alloy anodizing and casting methods on structure and functional properties," *Arch. Metall. Mater.* **61**(3), 991–996 (2016).
6. N. Uzan, I. Rosenthal, and A. Stern, "Macro- and microstructural characterization of cup-shaped AlSi10Mg components fabricated by selective laser melting (SLM)," *Metallogr. Microstruct. Anal.* **5**(6), 512–519 (2016).
7. G. Camicia and G. Timelli, "Grain refinement of gravity die cast secondary AlSi7Cu3Mg alloys for automotive cylinder heads," *Trans. Nonferrous Metals Soc. China* **26**(5), 1211–1221 (2016).
8. P. Saddei et al., "Detailed metallographic analysis of the surface layer structure of carbonitrided case-hardening steels after varied tempering treatments," *Pract. Metallogr.* **55**(3), 147–157 (2018).
9. Z. Kong et al., "Automatic tissue image segmentation based on image processing and deep learning," *J. Healthcare Eng.* **2019**, 2912458 (2019).
10. A. V. Logunov et al., "Investigation of SLZhS32 BR economically doped heat-resistant alloy with single-crystal structure," *Inorg. Mater. Appl. Res.* **7**(4), 564–569 (2016).
11. J. Qian et al., "Metallographic test of domestic PWR nuclear station spent fuel rod of 40 GWd/tU burnup," *Yuanzineng Kexue Jishu/At. Energy Sci. Technol.* **52**(3), 420–426 (2018).
12. Z. Cheng and S. Zhu, "Low stress fracture analysis of 30CrMnSiA steel cone part," *Jinshu Rechuli/Heat Treat. Metals* **43**(5), 240–242 (2018).
13. Z. Zhong and Y. Hu, "Detection of oxidation region of flexible integrated circuit substrate based on topology mapping," *Multimedia Tools Appl.* **78**(6), 7871–7892 (2019).
14. M. V. Chukin et al., "Structure and properties of carbon steel wire in drawing," *Steel Transl.* **48**(7), 441–445 (2018).

15. D. M. Fronczek et al., "Microstructure changes and phase growth occurring at the interface of the Al/Ti explosively welded and annealed joints," *J. Mater. Eng. Perform.* **25**(8), 3211–3217 (2016).

16. N. I. Polushin et al., "Influence of the matrix composition, structure, and properties on the service life of a diamond drilling tool," *Russ. J. Non-Ferrous Metals* **58**(2), 174–179 (2017).

17. M. V. Maisuradze and D. I. Lebedev, "The chemical composition effect of medium-carbon chromomanganesemolybdenum steel on the structure of drill pipes," *Steel Transl.* **49**(11), 813–818 (2019).

18. A. A. Smetkin et al., "Structure and properties of corrosion-resistant steels fabricated by selective laser melting," *Russ. J. Non-Ferrous Metals* **60**(6), 770–774 (2019).

19. O. V. Fomina, "Structure formation in high-strength nitrogen-bearing steel on hot deformation," *Steel Transl.* **47**(3), 172–177 (2017).

20. N. Ahmadi and G. Akbarizadeh, "Iris tissue recognition based on GLDM feature extraction and hybrid MLPNN-ICA classifier," *Neural Comput. Appl.* **32**, 2267–2281 (2020).

21. W. S. Qureshi et al., "Machine vision for counting fruit on mango tree canopies," *Precis. Agric.* **17**(3), 1–21 (2016).

22. S. Ghosal et al., "An explainable deep machine vision framework for plant stress phenotyping," *Proc. Natl. Acad. Sci. U. S. A.* **115**(18), 4613–4618 (2018).

23. A. A. Robie et al., "Machine vision methods for analyzing social interactions," *J. Exp. Biol.* **220**(1), 25–34 (2017).

24. L. Y. Chang et al., "Quantifying muskmelon fruit attributes with A-TEP-based model and machine vision measurement," *J. Integr. Agric.* **17**(006), 1369–1379 (2018).

25. C. Huang, "Particle swarm optimization in image processing of power flow learning distribution," *Discov. Internet Things* **1**, 12 (2021).

26. H. Wei, A. Sehgal, and N. Kehtarnavaz, "A deep learning-based smartphone app for real-time detection of retinal abnormalities in fundus images," *Proc. SPIE* **10996**, 1099602 (2019).

27. S. Cubero et al., "Automated systems based on machine vision for inspecting citrus fruits from the field to postharvest: a review," *Food Bioprocess Technol.* **9**(10), 1623–1639 (2016).

Keya Fu received his master's degree from PLA Navy Aviation University, Shandong, China. His research directions include image processing and machine learning.

Weibo Shi received his master's degree from China Institute of Metrology, Beijing, China. Currently, he is working in Luoyang Ship Material Research Institute. His research direction includes image processing and metallographic analysis.

Jiang Ke received his master's degree from Central South University, Changsha, China. Currently, he is working in Luoyang Ship Material Research Institute, Beijing. His research direction includes electronic information engineering.

Kai Guo received his doctoral degree from China University of Mining and Technology, Beijing. Currently, he is working in the School of Management, Henan University of Science and Technology, Luoyang, China. His research direction includes computational intelligence, management decision-making and optimization. He has published 51 academic papers and 5 books.